subbmission to Journal for Multiscale Computational Engineering

Multiscale model for temperature distribution in hydrating concrete

V. Šmilauer[1] and T.Krejčí[1]

Temperature rise in hydrating concrete presents a formidable problem which may lead to significant acceleration of hydration kinetics, early age cracking, and decreased durability. Multiscale formulation is proposed, coupling a cement hydration model on the microscale with the FEM heat conduction problem on the macroscale. While discrete hydration model predicts heat evolution controlled by macroscale temperature, FEM satisfies heat balance equation during thermal conduction. Two and three dimensional validation show a reasonable temperature agreement with an access to the local quantities such as the degree of hydration.

Keywords: *temperature, hydration heat, heat conduction, hydration model.*

1 Introduction

Concrete performance is affected by temperature history in many ways. Disregarding well-controlled laboratory conditions, mixing, placing and curing of concrete occur worldwide under varying environmental conditions. Understanding of underlying phenomena during concrete maturing and performance follows different attitudes of material and civil engineers and, in fact, presents a multiscale concept.

From a material point of view, concrete is a living heterogeneous material whose microstructure formation is affected by temperature considerably. It was recognized that higher curing temperature speeds up the rate of reactions and promotes high early strength [Neville, 1997]. However, such microstructure is characteristic by inhomogeneous placing of hydrates, coarser porosity, and denser calcium silicate hydrates (C-S-H) [Lothenbach et al., 2008], resulting in a decreased long-term strength and durability. Remarkable advancement in high-strength concrete, utilization of secondary cementitious materials (SCM) and the use of admixtures has made concrete material even more complex [Bentur and Mitchell, 2008].

[1]CTU in Prague, Faculty of Civil Engineering, Dept. of Mechanics, Thákurova 7, 166 29 Prague 6, Czech Republic, tel. +420 224 354 369, fax. 224 310 775, e-mail: vit.smilauer@fsv.cvut.cz, krejci@fsv.cvut.cz

Prediction of thermal stresses based on temperature history is a well established concept in the framework of structural mechanics. A low thermal conductivity of concrete, exothermic hydration process and surrounding temperature cause temperature gradients accompanied by strains, especially in massive concrete members. During concrete cooling, tensile stresses often appear due to minor restraints in the system which may lead to a microcrack formation and decreased durability [Nilsson, 2000, Schrage and Summer, 1994].

Several researchers formulated predictive models for temperature evolution under adiabatic condition; in the form of exponential function [Wang and Dilger, 1994], or hydration model [Bentz et al., 1998]. Proper validation became a stepping stone for a multiscale approach, recognizing the heterogeneous temperature distribution on the macroscale. Coupled micro/macro analysis followed either phenomenological hydration model [Estrada et al., 2006] or more sophisticated affinity hydration model [Park et al., 2008].

The formulation of fully coupled thermo-chemo-mechanical models was nevertheless proposed [Ch. Hellmich, 2001, Gawin et al., 2006a, Gawin et al., 2006b, Ulm and Coussy, 1998] and is remarkable for the amount of input parameters. Several of them have to be obtained experimentally, weakening the potential for a general-purpose tool.

Instead of direct modeling the crack formation using highly sophisticated models, engineers often proposed guidelines to produce high quality concrete satisfying elementary rules [Neville, 1997, NRMCA, 2007]. Such approach does not require detailed modeling and relies more on experience and expertise. For example, the temperature anywhere in concrete member should not exceed 70 °C during hardening due to possible risk in delayed ettringite formation causing later expansion [Barbarulo et al., 2005]. Cooling rate should not exceed 3 °C per hour during the first 24 hours or special caution is necessary in cold weather when concrete temperature falls bellow 4 °C [NRMCA, 2007].

This paper presents thermo-chemical multiscale model to predict realistic temperature evolution and distribution in arbitrary concrete member under varying boundary conditions. The emphasis is given on the material scale, taking into account cement chemical and physical properties. Discrete CEMHYD3D hydration model based on cellular automata is used to simulate microstructure evolution of hydrating cement paste [Bentz, 2005]. Conventional transient heat conduction problem is solved by means of FEM at the macroscale level [Wang and Mai, 2005]. The formulation relies on intrinsic material data, such as reaction enthalpy, resulting in a versatile and extensible engineering tool.

2 Coupling micro and macro scale

The multiscale nature of concrete structures allows to identify two separable scales, each with specific behavior

cement paste level found on the scale between 1 μm and 100 μm. Clinker minerals, gypsum, CH, C-S-H, other minor phases, and capillary porosity are present,

structural level represents the span from centimeter up to several meters. Concrete found at this level is comprised mainly from cement paste, SCM, fine and coarse aggregates. The topology of concrete structure with assigned boundary conditions complement material information.

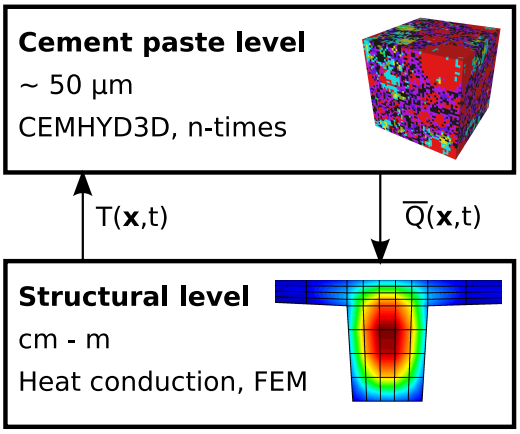

Figure 1: Coupling between cement paste and structural level

Fig. 1 displays adopted coupling between two scales. The heat source $\overline{Q}(\mathbf{x}, t)$ represents the hydration heat of cement paste determined from the CEMHYD3D model on the microscale scale. Since temperature has a strong effect on released heat, it becomes necessary to couple hydration model on the microscale with the structural model on the macroscale in terms of temperature and liberated hydration heat.

Instead of having separate microstructures in each Gauss points, they can be assigned directly to finite element(s) or a broader selection. The temperature for CEMHYD3D is taken as an average from corresponding Gauss points. Such simplification is advantageous in reduced computational time when finite elements are expected to exhibit similar temperature field. The multiscale model is implemented in a general FEM open-source package TRFEL[2] suited for transport problems.

[2]http://mech.fsv.cvut.cz/ ~sifel

3 Cement hydration model on the microscale

It is assumed that aggregates in concrete do not contribute significantly to the cement hydration process, therefore the heat evolution of concrete may be obtained directly from the cement paste level. Realistic modeling of elementary chemical reactions associated with hydration and cement grain size distribution call for a sophisticated hydration model. An open-source, discrete hydration model CEMHYD3D [Bentz, 2005] was adapted, allowing to include directly

- particle size distribution of cement,
- chemical composition of cement (C_3S, C_2S, C_3A, C_4AF, gypsum),
- actual temperature and its history,
- water regime (saturated and sealed conditions),
- water-to-cement ratio (w/c) and the amount of cement in concrete,
- supplementary cementitious materials (silica, slag, fly ash).

The microstructure of cement paste, referring to as a representative volume element (RVE), is approximated by voxels with the size of $1 \times 1 \times 1$ μm. Each of them represents one chemical phase, either in solid or dissolved state. Fig. 2 shows an example of initial and well hydrated RVE of $50 \times 50 \times 50$ μm. The initial periodic RVE is reconstructed by throwing digital spheres following cement particle size distribution (PSD). A reference database of NIST cements, see [Bentz, 2005], allowed to approximate PSD by Blaine fineness. Rosin-Rammler cumulative distribution $G(d)$ is assumed leading, after the fit to the database data, to

$$G(d) = 1 - e^{-bd^n}, \quad \lim_{d\to\infty} G(d) = 1, \tag{1}$$

$$n = -8.333 \cdot 10^{-4}\,\text{fineness} + 1.1175, \tag{2}$$

$$b = 7.54 \cdot 10^{-4}\,\text{fineness} - 0.143, \tag{3}$$

where d [μm] is the particle diameter and Blaine fineness is expressed in [m^2/kg]. The amount of cement in the RVE is controlled by w/c and gypsum content.

The chemical reactions are modeled on the basis of cellular automata rules, describing the process of dissolution, transport, nucleation, and reaction. Liberated heat is calculated directly from evolving microstructure assigning enthalpy to each chemical reaction [Bentz et al., 1998]. For example, the reaction of the most common mineral C_3S of Portland cement yields 517 J/g of reacted C_3S

$$C_3S(1) + 5.3H(1.34) \rightarrow C_{1.7}SH_4(1.52) + 1.3CH(0.61), \tag{4}$$

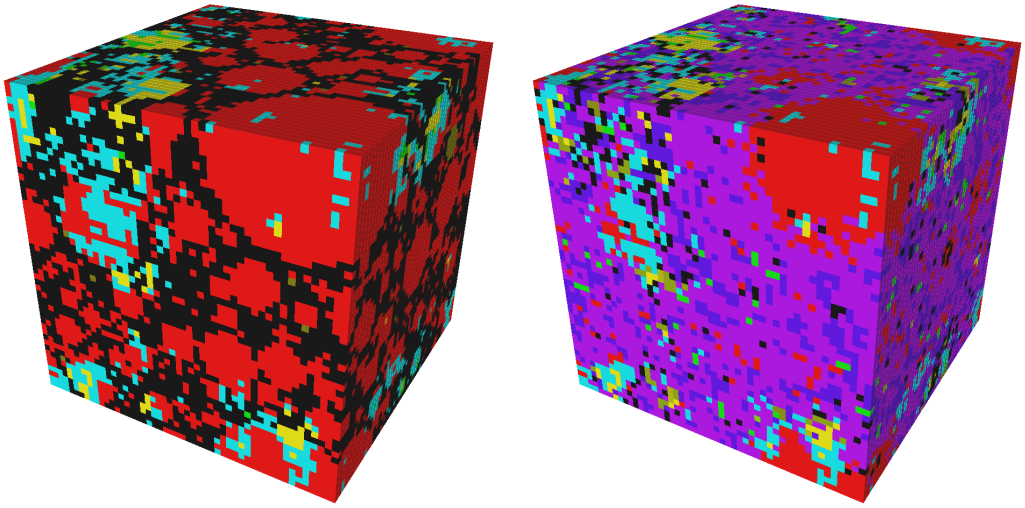

Figure 2: RVE $50 \times 50 \times 50$ μm, $w/c = 0.25$, initial (left) and at the degree of hydration of 0.63 (right). Water-filled porosity, C_3S, C_2S, C_3A, C_4AF, gypsum, and hydration products are distinguished

where the numbers in parenthesis correspond to reaction volumes at 20 °C. Saturated or sealed curing conditions are considered in the model with no further moisture effect on hydration. Such simplification is supported by the fact that relative humidity (RH) seldom drops below 90 % even in exterior parts within a few days when exposed to 60 % RH [Neville, 1997]. Therefore, sealed curing boundary condition is a realistic assumption when no considerable water evaporation takes place. If RH drops bellow approximately 80 % RH, the hydration ceases.

The temperature effect on hydration kinetics is determined from Arrhenius equation simultaneously for all implemented reactions. The characteristic time τ is modified according to the maturity principle [Maekawa et al., 1999]

$$\tau(T) = \tau(T_0) \exp\left[\frac{E_a}{R}\left(\frac{1}{T_0} - \frac{1}{T}\right)\right], \tag{5}$$

where $T_0 = 298.15$ K is a reference temperature, T corresponds to arbitrary homogeneous temperature, $R = 8.314$ Jmol^{-1}K^{-1} represents the universal gas constant and E_a stands for an apparent activation energy, typically around 40 kJmol^{-1} for ordinary Portland cement [Kada-Benameur et al., 2000]. Eq. (5) demonstrates a strong temperature effect on heat release, e.g. going from 25 to 50 °C is a speedup by the factor of 3.5 for hydration progress and heat release rate.

The cycles in cellular automata represent no meaningful scale of time. Original linear mapping of cycles showed considerable disagreements with experiments [Bentz, 2000]. Parabolic mapping, based on the Knudsen's parabolic dispersion model, was found appropriate under different curing conditions and cement types [Bentz, 1995]. Knudsen's model assumes that the diffusion of ions takes the control over the hydration rate

$$\tau = t_0 + \beta \, \mathrm{cycle}^2. \tag{6}$$

The parameter β is usually found in the interval $1 \cdot 10^{-4} \leq \beta \leq 1.1 \cdot 10^{-3}$ h [Bentz, 1995, Bentz et al., 1999] expressing the influence of admixtures, alkalis etc., while t_0 represents the latency of dormant period.

The size of RVE plays a fundamental role in the calculations [Kanit et al., 2003]. For the cement hydration, one has to consider at least the effect of truncated particle size distribution, cement fineness, and w/c. Microstructure reconstruction as well as cellular automata are governed by random numbers, therefore five random realizations were carried out to highlight the effect of RVE size.

Fig. 3 displays the evolution of degree of hydration, tightly related to released heat, for ordinary Portland coarse cement with Blaine fineness 250 m^2/kg and $w/c = 0.5$. The maximum accommodated particle diameter is truncated to a half of RVE edge, i.e. to diameter 5 μm at $10 \times 10 \times 10$ and 25 μm at $50 \times 50 \times 50$ μm. Hydration at 20 °C shows that $10 \times 10 \times 10$ μm proceeds faster due to truncated large particles than reference at $100 \times 100 \times 100$ μm. The reasonable selection is $50 \times 50 \times 50$ μm for the scatter and computational speed.

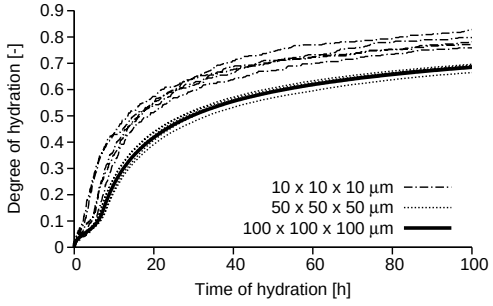

Figure 3: The effect of RVE sizes on degree of hydration, each with five random realizations

Nowadays, SCM such as slag or fly ash are blended with Portland cement due to economical, ecological and durability reasons. The common level of substitution reaches up to 35 % by mass, although much higher replacements

may exist [Neville, 1997]. The consequence is decreased potential heat of blended cement with slow transformation of secondary binders to hydration products. Since very low heat contribution, if any, from the reaction of SCM generally occurs during first hydration days [Pane and Hansen, 2005, Papadakis, 1999, Robeyst et al., 2007, Snelson et al., 2008], the SCM is considered as an inert filler in the simulations.

4 Mathematical formulation of heat transport

Transient 3D heat conduction problem in incompressible media can be derived from an energy balance on a differential element [Lienhard and Lienhard, 2008, Wang and Mai, 2005]

$$-\nabla^T \mathbf{q}(\mathbf{x}) + \overline{Q}(\mathbf{x}, t) = \rho(\mathbf{x}) c_p(\mathbf{x}) \frac{\partial T(\mathbf{x}, t)}{\partial t} \tag{7}$$

where $\mathbf{q}(\mathbf{x})$ [W/m^2] is a heat flux originating in conduction, convection, or radiation, $\overline{Q}(\mathbf{x}, t)$ [W/m^3] represents known heat source from CEMHYD3D model, $\rho(\mathbf{x})$ [kg/m^3] stands for a material density, $c_p(\mathbf{x})$ [Jkg^{-1}K^{-1}] is a specific heat capacity and $T(\mathbf{x}, t)$ [K] represents unknown temperature field. The derivation will further consider an isotropic material.

The heat flux may be obtained from three basic modes. The first mode corresponds to a heat conduction expressed by Fourier's law on a differential element

$$\mathbf{q}(\mathbf{x}) = -\lambda(\mathbf{x}) \nabla T(\mathbf{x}), \tag{8}$$

where $\lambda(\mathbf{x})$ [Wm^{-1}K^{-1}] is the thermal conductivity of isotropic material.

Inserting Eq. (8) in Eq. (7) leads to the formulation of 3D heat conduction of parabolic type equation in terms of temperature field

$$\lambda(\mathbf{x}) \Delta T(\mathbf{x}) + \overline{Q}(\mathbf{x}, t) = \rho(\mathbf{x}) c_p(\mathbf{x}) \frac{\partial T(\mathbf{x}, t)}{\partial t} \tag{9}$$

The second mode represents a heat convection. One can consider concrete surface exposed to air. The air flows around the concrete body and forms a thin region called a boundary layer. The convection process occurs inside the layer and sweeps the heat from concrete surface farther. The heat flux is described by Newton's law on the body surface

$$\mathbf{n}(\mathbf{x})^T \mathbf{q}(\mathbf{x}) = h(\mathbf{x}) \left(T(\mathbf{x}) - T_\infty \right), \quad \mathbf{x} \in \Gamma_c, \tag{10}$$

where $\mathbf{n}(\mathbf{x})$ is a unit normal vector pointing outwards from the surface, $h(\mathbf{x})$ [$\mathrm{Wm^{-2}K^{-1}}$] is a heat transfer coefficient and T_∞ is the ambient temperature far enough from the boundary layer.

The third mode describes heat transfer by thermal radiation. Stefan-Boltzmann law on the body surface reads

$$\mathbf{n}(\mathbf{x})^T\mathbf{q}(\mathbf{x}) = \varepsilon(\mathbf{x})\sigma(\mathbf{x})\left(T^4(\mathbf{x}) - T_\infty^4\right), \quad \mathbf{x} \in \Gamma_r, \tag{11}$$

where $\varepsilon(\mathbf{x})$ is an emittance in the range $\langle 0, 1\rangle$, and $\sigma(\mathbf{x}) = 5.67 \cdot 10^{-8}$ [$\mathrm{Wm^{-2}K^{-4}}$] stands for Stefan-Boltzmann constant. The emittance of rough concrete is 0.94 at 40 °C [Lienhard and Lienhard, 2008].

The solution of Eq. (9) requires prescribed initial temperature $\overline{T}(\mathbf{x}, 0)$ over the body

$$T(\mathbf{x}, 0) = \overline{T}(\mathbf{x}, 0), \quad \mathbf{x} \in \Omega. \tag{12}$$

The differential Eq. (9) has to be complemented further with boundary conditions which have a variety of forms. Dirichlet's boundary condition prescribes temperature

$$T(\mathbf{x}, t) = \overline{T}(\mathbf{x}, t), \quad \mathbf{x} \in \Gamma_T, \tag{13}$$

Neumann's boundary condition specifies heat flux either non-linear such as Eq. (11) or linear with prescribed flux $\overline{q}(\mathbf{x}, t)$

$$\mathbf{n}(\mathbf{x})^T\mathbf{q}(\mathbf{x}, t) = \overline{q}(\mathbf{x}, t), \quad \mathbf{x} \in \Gamma_{\overline{q}}, \tag{14}$$

while Cauchy's boundary condition represents generally a mixed condition, for example Newton's law in Eq. (10).

4.1 Solution by FEM

The analytical solution of Eq. (9) is not amenable for more complicated cases. Instead, FEM is employed, starting with the formulation of a weak problem [Wang and Mai, 2005]. To simplify the solution, radiation on Γ_r will not be considered and the linear set of algebraic equations will be obtained in the form

$$\boldsymbol{C}\dot{\mathbf{r}} + \boldsymbol{K}\mathbf{r} = \mathbf{p}, \tag{15}$$

where $\dot{\mathbf{r}}$ are temperature nodal derivatives with respect to time. Element matrices and heat load vector $\mathbf{p}$ are provided by

$$\boldsymbol{C} = \int_{\Omega} \boldsymbol{N}(\mathbf{x})^T \rho(\mathbf{x}) c_p(\mathbf{x}) \boldsymbol{N}(\mathbf{x}) \mathrm{d}\Omega, \tag{16}$$

$$\boldsymbol{K} = \int_{\Omega} \boldsymbol{B}(\mathbf{x})^T \lambda(\mathbf{x}) \boldsymbol{B}(\mathbf{x}) \mathrm{d}\Omega, \tag{17}$$

$$\mathbf{p} = -\int_{\Gamma_{c,T,\overline{q}}} \boldsymbol{N}(\mathbf{x})^T \mathbf{q}(\mathbf{x},t) \mathrm{d}\Gamma + \int_{\Omega} \boldsymbol{N}(\mathbf{x})^T \overline{\mathbf{Q}}(\mathbf{x},t) \mathrm{d}\Omega. \tag{18}$$

The heat load vector in Eq. (18) comprises heat flow and heat source. The solution of first-order transient problem of Eq. (15) can be accomplished by many techniques, e.g. finite differences or mode superposition. The attention is focused to a generalized trapezoidal method where the time domain is discretized by a time step

$$\Delta t_n = t_{n+1} - t_n, \quad n = 1, 2 \ldots (\text{time steps} - 1), \tag{19}$$

and the solution proceeds by the v-form of trapezoidal scheme described in [Hughes, 2000]. Crank-Nicolson integration scheme is used further. It should be noted that heat source $\overline{Q}(\mathbf{x}, t_{n+1})$ is determined from average temperature at the previous time step t_n thus bringing small inaccuracy which remains in the calculation.

5 Thermal properties of concrete

The simulation of heat conduction problem requires concrete heat conductivity, capacity and heat transfer coefficient. Hydration process changes the volume fraction of evaporable water, unhydrated cement and hydrates. Therefore, thermal properties vary with concrete composition and degree of hydration. Fig. 4 displays data for mature ordinary concrete depending on concrete unit mass and saturation conditions according to [Neville, 1997] and former Czech standard ČSN 731208. The latter considers 1.5 for dry and 1.7 $\mathrm{Wm^{-1}K^{-1}}$ for water saturated concrete.

Concrete can be considered at the first approximation as a two phase medium comprising cement paste and aggregates. Heat capacity of cement paste is significantly affected by the amount of water with heat capacity 4.187 $\mathrm{Jg^{-1}K^{-1}}$. The cement powder has typically 0.75 $\mathrm{Jg^{-1}K^{-1}}$ [Bentz, 2008]. Detailed study found that fresh cement paste corresponds to heat capacities 1.55, 1.73, 1.89 $\mathrm{Jg^{-1}K^{-1}}$ for $w/c = 0.3, 0.4$ and 0.5, respectively [Bentz, 2008]. The law of mixture can be used for the estimation of heat capacity

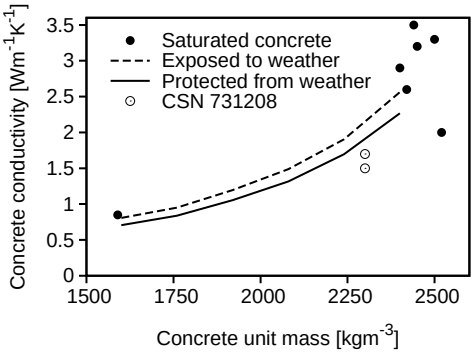

Figure 4: Thermal conductivity of mature concrete

for concrete. Fig. 5 shows the result according to [Bentz, 2008] for cement paste and concrete made from the paste with 85 % of granite aggregate by mass. Former Czech standard ČSN 731208 declares 0.84 and 0.87 $\mathrm{Jg^{-1}K^{-1}}$ for dry and saturated mature concrete, respectively.

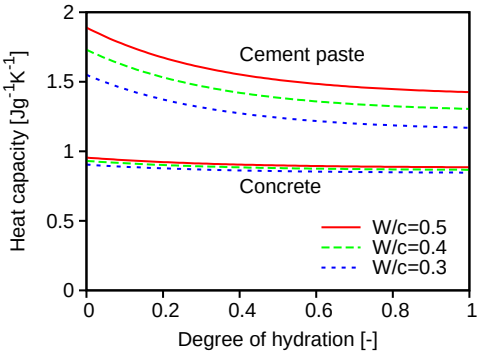

Figure 5: Heat capacity for cement paste and concrete

Different heat transfer coefficients were reported in the literature, e.g. [Park et al., 2008] considered $h = 11.63$ $\mathrm{Wm^{-2}K^{-1}}$ for concrete exposed to air while $h = 9.3$ $\mathrm{Wm^{-2}K^{-1}}$ for the surface surrounded by plywood formwork. [Estrada et al., 2006] used $h = 9.7$ $\mathrm{Wm^{-2}K^{-1}}$ for the heat transfer between formwork and ambient air. Tab. 1 summarizes heat transfer coefficient for concrete according to a former Czech standard ČSN 731208. When concrete surface is covered with other layers of materials, such as a formwork, heat transfer coefficients add inversely. The overall heat transfer coefficient is a harmonic mean

$$h_i = \frac{\lambda_i}{t_i}, \tag{20}$$

$$\frac{1}{h} = \sum_{i=1}^{n} \frac{1}{h_i} = \frac{1}{h_1} + \frac{t_2}{\lambda_2} + \dots, \tag{21}$$

where t is the thickness of layer.

Table 1: Heat transfer coefficient for concrete exposed to air or water according to the standard ČSN 731208

Concrete in contact with	h [$\mathrm{Wm^{-2}K^{-1}}$]
air in enclosed environment	8
air during summer	15
air during winter	23
water	31

6 Validation

6.1 Isothermal calorimetry of cement paste

Validation of CEMHYD3D starts on a paste prepared from ordinary Portland cement CEM I 42.5 R, produced at location Mokrá, Czech republic. Cement was mixed with water at $w/c = 0.5$ and inserted in isothermal calorimeter at 25 °C. CEMHYD3D model was calibrated for parameters β and t_0 according to Eq. (6). Initial RVE of size $50 \times 50 \times 50$ μm was reconstructed and hydrated with input parameters summarized in Tab. 2.

Table 2: Cement properties and simulation parameters

Component	C_3S	C_2S	C_3A	C_4AF	Gypsum
Mass content without gypsum	0.612	0.126	0.070	0.10	-
Normalized mass content without gypsum	0.683	0.138	0.083	0.096	-
Volume content with gypsum	0.649	0.131	0.078	0.092	0.05
Blaine fineness	306 $\mathrm{m^2/kg}$				
Autocorrelation NIST files	cm115x2f				

The calibration provided $\beta = 7.8 \cdot 10^{-4}$ h and $t_0 = 1.2$ h. Reference and experimental temperatures are the same hence the activation energy is irrelevant. Results in Fig. 6 exhibit small discrepancy in the beginning

of hydration due to the assumptions of C-S-H control over kinetics [Bentz et al., 1999]. Time period after 10 hour is modeled properly. A discrepancy at later hydration stage may be attributed to the sensitivity and stability of the calorimeter unit. Potential hydration heat Q_{pot} corresponds to 520.54 J/g of cement.

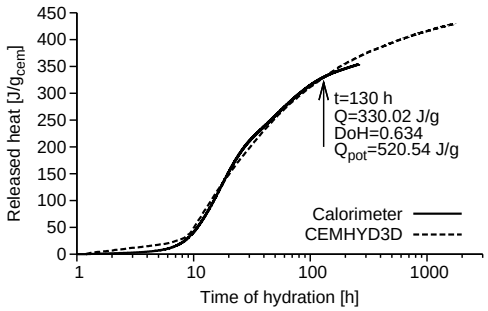

Figure 6: Isothermal calorimetry and CEMHYD3D simulation at 25 °C, $w/c = 0.5$

6.2 Cube of self compacting concrete

The temperature evolution of self-compacting concrete was measured at Czech Technical University in Prague. A cube of 1 × 1 × 1 m was casted at one step in the shelter protecting the specimen from sun radiation and rain. Nine equally spaced temperature gages were embedded in the horizontal direction across the cube thickness, the outer sensor was placed 30 mm from the surface, Fig. 7. Two temperature gages measured ambient air temperature and all data were automatically gathered for the duration of at least six days.

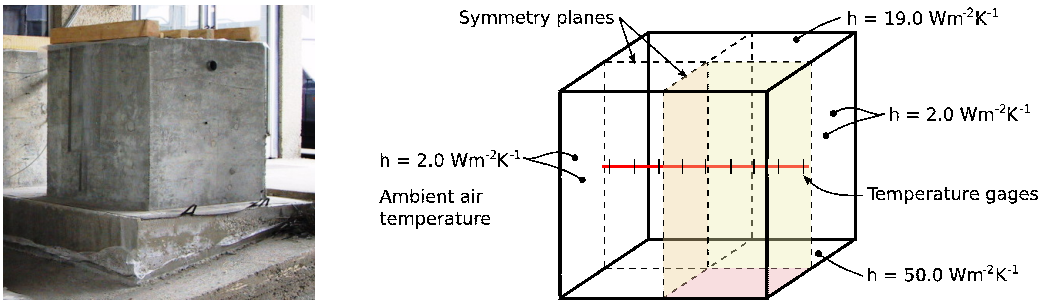

Figure 7: Experimental setup and corresponding model (photo J. Litoš)

The model description is given by Fig. 7. The top surface was in direct contact with atmosphere, therefore the heat transfer coefficient was chosen $h = 19$ Wm^{-2}K^{-1} as the average between winter and summer season, Tab. 1. The thickness of formwork plywood in the vertical direction was 15 mm, therefore

$$h = \left(\frac{1}{19} + \frac{0.015}{0.13} \right)^{-1} = 5.95 \text{ Wm}^{-2}\text{K}^{-1}. \tag{22}$$

During pilot simulation, the difference between center and surface temperature revealed that the coefficient has to be much lower and the value of 2.0 Wm^{-2}K^{-1} was assumed instead.

The cube was placed on an old massive concrete separated by 2 mm thick impregnated paper, therefore

$$h = \frac{\lambda}{t} = \frac{0.1}{0.002} = 50.0 \text{ Wm}^{-2}\text{K}^{-1} \tag{23}$$

and the old concrete was considered conservatively to have the temperature of ambient air.

Symmetrical configuration allowed to simulate a cube quarter only. The prism was meshed for $2 \times 2 \times 4 = 16$ quadratic brick elements, the mesh had 141 DoF. One CEMHYD3D model was assigned to each finite element. Time integration step was chosen fixed as 10 minutes.

The concrete was composed from CEM I 42.5 R by the amount of 310 kg/m^3 with $w/c = 0.4$. Fly ash as a filler was added further to the mixture but was disregarded for the heat contribution. Since cement mineralogical properties were unknown, data for initial microstructure were taken from Tab. 2 from an ordinary Portland cement of the same grade with the activation energy $\text{E}_\text{a} = 38.3$ kJ/mol. Thermal conductivity of concrete was assumed constant 1.7 Wm^{-1}K^{-1}, its capacity constant 0.84 Jg^{-1}K^{-1}, and density 2.5 t/m^3.

Fig. 8 shows the temperature evolution in the middle of the cubic specimen and ambient air temperature. Following parameters were calibrated to match experimental data; $t_0 = 0$ h and $\beta = 6.3 \cdot 10^{-4}$ h from Eq. (6). The maximum temperature in the center reached 50.17 °C at 25.6 hours and the simulation predicted 50.3 °C. Maximum temperature achieved 30 mm from the surface was 45.23 °C and the simulation predicted 44.3 °C. The cooling stage after approximately two days shows overprediction by the simulation and emphasizes the role of heat transfer coefficients. A part of heat could have dissipated from water evaporation which was not taken into account. Fig. 9 shows contour fill of prism viewed from the central direction during

the maximum center temperature at 25.6 hours. Total computational time took 70 minutes on 3.2 GHz PC with optimized g++ compilation. Profiling showed that 98.5 % of the whole computational time is taken by CEMHYD3D routine. In such particular case, no time savings are caused by the refinement of integration time step.

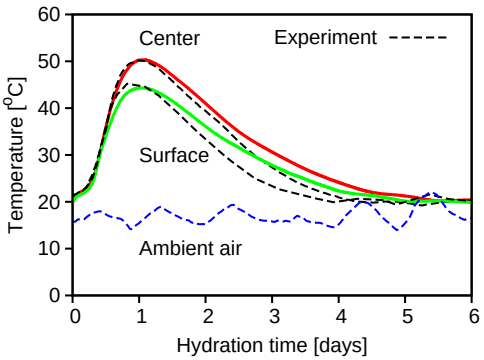

Figure 8: Validated heat evolution in the 1 × 1 × 1 m specimen

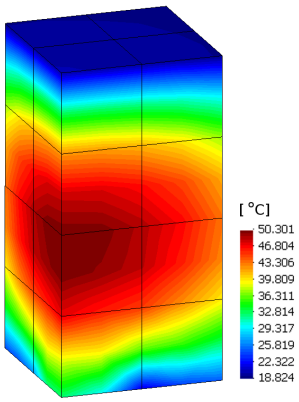

Figure 9: Contour fill of temperature field at 25.6 hours

6.3 Prestressed railway bridge in Prague

A new railway scaffold bridge had been built during 2006-2007 in the Prague city center, Fig. 10. The bridge is a continuous beam of 12 spans made from prestressed concrete with the total length of 443 m.

Figure 10: Construction of railway scaffold bridge (photo D. Prause)

The first simulation deals with the casting of bottom slab of the thickness of 0.697 m with a precast shoulder. The mesh was generated by T3D[3] software with resulting 215 nodes, 4 triangular and 179 quadrilateral elements, together with 215 DoF, Fig. 11. The horizontal layered mesh structure was preferred due to CEMHYD3D assignment. Each layer of 20 elements has a similar temperature fields therefore these elements are grouped to eight independent CEMHYD3D models according to Fig. 11.

The casting began at 10:00 on Jun 06, 2006. Initial temperature of casted concrete was measured in the interval 14.1 – 15.7 °C, therefore was set to initial 15 °C together with the precast shoulder. Both casted concrete and precast shoulder were given the constant material parameters; thermal conductivity 1.7 $\mathrm{Wm^{-1}K^{-1}}$ and the heat capacity 0.84 $\mathrm{Jg^{-1}K^{-1}}$. Used concrete composition with $w/b = 0.425$ is summarized in Tab. 3.

Pilot simulation revealed that the amount of Portland cement is excessive and has to be reduced to the minimum value 95 % according to EN197-1, i.e.

[3]http://mech.fsv.cvut.cz/~dr/t3d.html

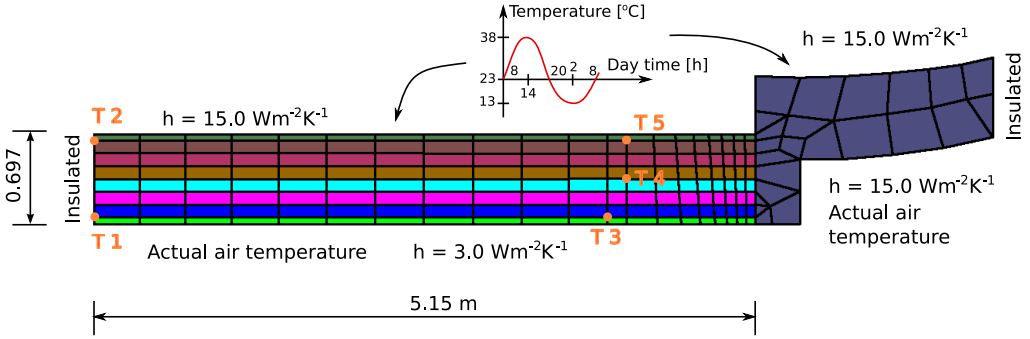

Figure 11: Mesh and boundary conditions of bottom slab. Different colors mean eight CEMHYD3D material models, the right shoulder is made from mature precast concrete

Table 3: Concrete composition used in the simulation of the bridge, $w/b = 0.425$.

Concrete parameter	Value
Type	C35/45-XF2
Cement (CEM I 42.5 R + SCM)	380+20 kg/m^3
Water	170 kg/m^3
Fine aggregates	1100 kg/m^3
Coarse aggregates	450 kg/m^3
Fly ash	200 kg/m^3
Superplasticizer	3.6 kg
Bulk density	2.32 kg/m^3

280 kg of pure Portland cement and 20 kg of inert SCM admixtures, yielding $w/c = 170/380 = 0.4473$. Input parameters were assumed according to Tab. 4 with $t_0 = 0$ h and $\beta = 5.6 \cdot 10^{-4}$ h. Boundary conditions were set according to Fig. 11. While the bottom part was set to measured air ambient temperature, the temperature of top surface, exposed to sun radiation, was approximated by

$$T(t) = 23 + \left[10 + 5 \cdot H\left(\sin\left\{2\pi t + \frac{4\pi}{24}\right\}\right)\right] \cdot \sin\left\{2\pi t + \frac{4\pi}{24}\right\}, \qquad (24)$$

where $H(\ )$ is a Heaviside step function and time t is in days relatively to the beginning of casting. The maximum air temperature was considered at 14.00 h according to measured data.

Table 4: Cement properties and material simulation parameters

Component	C_3S	C_2S	C_3A	C_4AF	Gypsum
Mass content without gypsum	0.65	0.15	0.10	0.10	-
Volume content with gypsum	0.6175	0.1425	0.095	0.095	0.05
Blaine fineness	300 m^2/kg				
Autocorrelation NIST files	16130s1				
Activation energy E_a	38.3 kJ/mol				

Similar location of gages T1 – T3 and T2 – T5 gives very similar evolution of temperatures. Results for inner gage T4 and ambient air temperature are plotted in Fig. 12, Fig. 13 shows gages T3, T5. The inner part of casted massive concrete is close to adiabatic condition and is influenced to a minor extent by boundary conditions. Therefore, the correspondence between simulation and experiment reveal appropriate selection of material parameters. Data from ambient air temperature are incomplete and the results between two points are interpolated in the simulation.

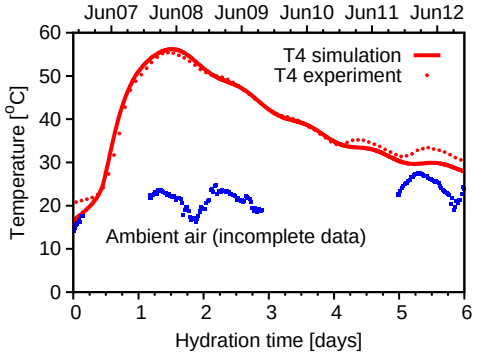

Figure 12: Temperature of central gage T4 and ambient temperature

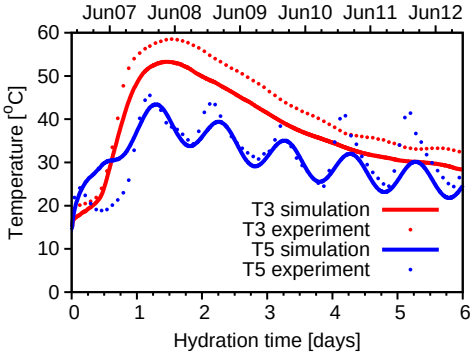

Figure 13: Temperature evolution of gages T3 and T5

The maximum temperature 56.2 °C was reached in gage T4 at 1.53 day and the temperature field is plotted in Fig. 14. Whole simulation took 57 minutes on 3.2 GHz PC and occupied 29 MB of RAM. Total simulation covered six days of hydration period with the constant time integration step 10 minutes.

New bridge beams had been casted on the bottom slab since Jul 12, 2006 6:39 AM, i.e. after 35 days of bottom slab casting. A maximum beam width was 1.65 m and height 2.15 m. The generated mesh had 239 nodes, 39 triangular and 177 quadrilateral elements with total 239 DoF. A simulated, typical cross section is depicted in Fig. 15 and allows to consider again bridge

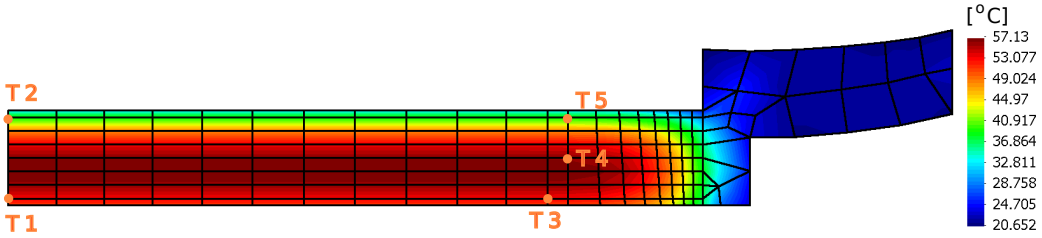

Figure 14: Contour fill at maximum temperature 56.2 °C in gage T4 after 1.53 day

symmetry vertical axis. Although the data from gages T1-T5 were gathered from the bottom slab, only gage T5 was considered important from maturing concrete slab. The mesh was adjusted in such a way that gages T5 – T10 were forced to be at a nodal position. The assignment of five hydration models with expected similar temperature field is displayed in Fig. 15.

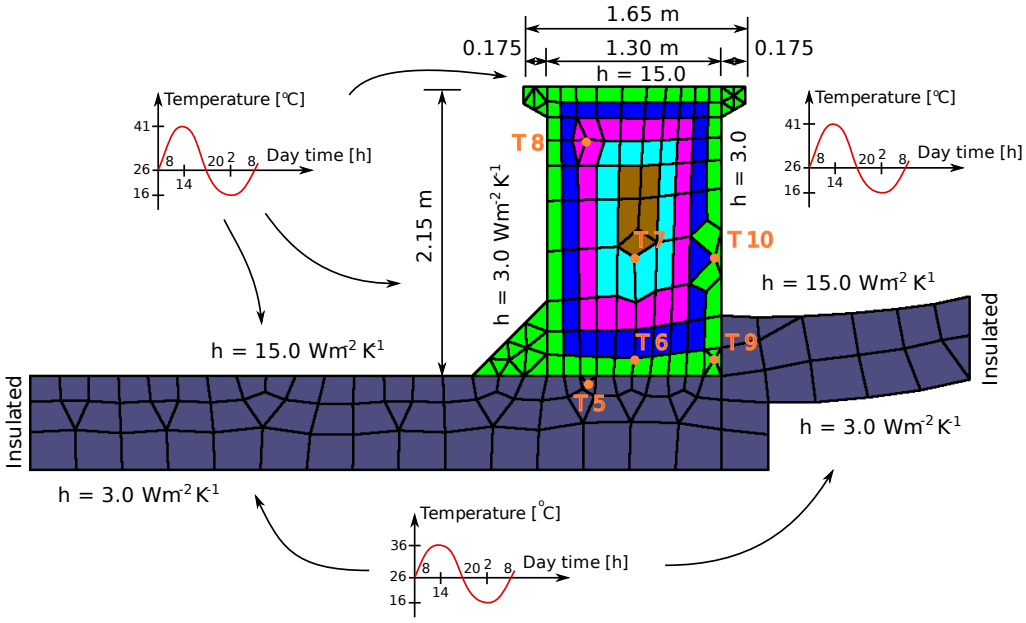

Figure 15: Topology and boundary conditions of the beam. Different colors represent different CEMHYD3D material models, the right shoulder and bottom slab are considered non-hydrating

The initial ambient air temperature was 26 °C, mature and fresh casted concrete had 25 °C. The time functions of bottom ambient air temperature

were prescribed by the function

$$T(t) = 26 + 10 \sin\left\{2\pi t - \frac{2.7\pi}{24}\right\}, \tag{25}$$

and the upper and vertical surfaces

$$T(t) = 26 + \left[10 + 5 \cdot H\left(\sin\left\{2\pi t - \frac{2.7\pi}{24}\right\}\right)\right] \cdot \sin\left\{2\pi t - \frac{2.7\pi}{24}\right\}. \tag{26}$$

Concrete and simulation parameters were set according to Tabs. 3, 4. Further calibration modified $t_0 = 3$ h and $\beta = 4.0 \cdot 10^{-4}$ h. The pair gages T6–T7, T9–T10 gave very similar experimental results, therefore only gages T5, T7, T10 were validated.

Results for the central gage T7 are in Fig. 16. Maximum temperature was not measured directly due to power disconnection, however, the simulated temperature reached maximum 86.8 °C at 1.367 days, Fig. 18. Good agreement is achieved in T5 and T10 as well, Fig. 17. Both figures show temperature underestimation probably due to lower heat transfer coefficients on the surfaces. Whole beam simulation took 68 minutes on 3.2 GHz PC and occupied 19 MB of RAM. Calculations covered 10 days of hydration period with a constant time integration step 10 minutes using the Crank-Nicolson scheme.

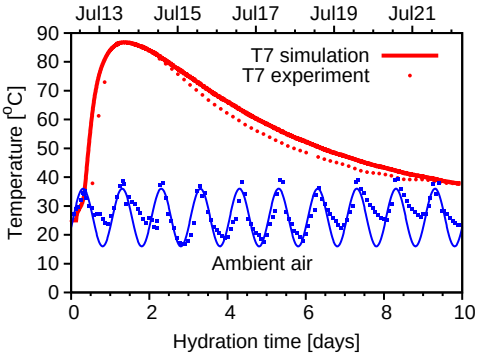

Figure 16: Temperature of central gage T7 and approximated ambient air

Multiscale formulation allows accessing local quantities. The evolution of hydration degrees is depicted in Fig. 19 and demonstrates the effect of temperature history. Ultimate hydration degree approaches to 0.8 due to low cement fineness hence the inability to hydrate large cement grains completely. Young's modulus can be predicted on the scale of cement paste and concrete.

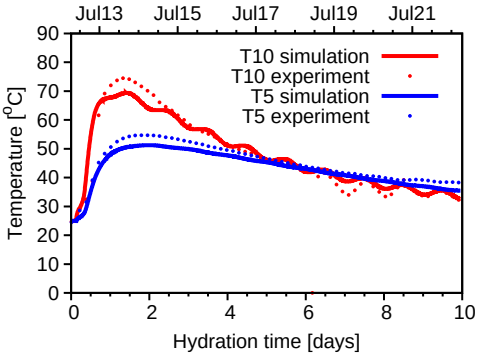

Figure 17: Temperature evolution in gages T3 and T5

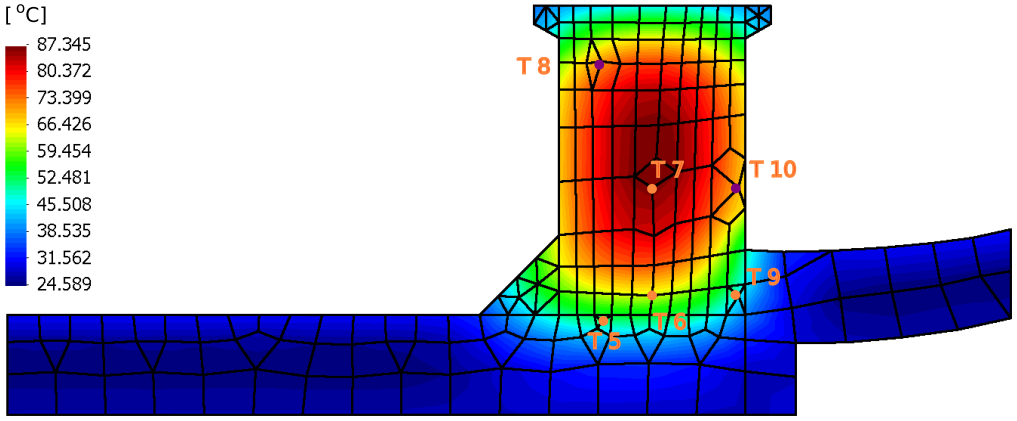

Figure 18: Temperature field at 1.367 days

Analytical homogenization process adopted here is similar to [Bernard et al., 2003], relying on intrinsic elastic properties of clinker minerals, hydration products and aggregates. In addition, homogenization includes the effect of interfacial transition zone, two types of C-S-H [Šmilauer and Bittnar, 2006] and entrained air. Typical values complementing known concrete composition in Tab. 3 were used and the results are plotted in Fig. 20. Subtle differences are observed in both gages due to the fact that effective Young's modulus in tightly related to degree of hydration. Both results are even closer due to the fact that C-S-H have higher molar volume at lower temperature, partially substituting porosity reduction due to hydration progress.

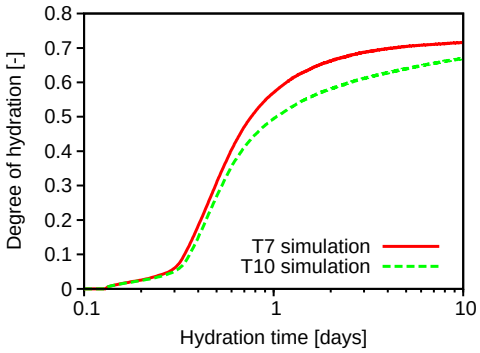

Figure 19: Evolution of hydration degree in gages T7, T10

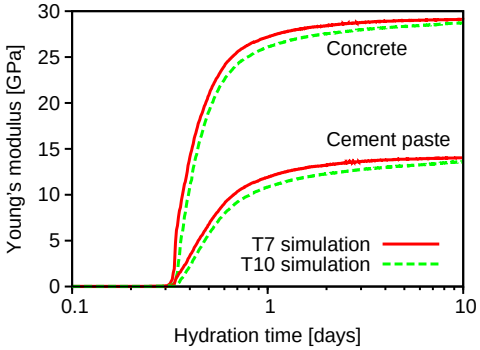

Figure 20: Evolution of Young's modulus in gages T7, T10 on the scale of cement paste and concrete

6.4 Role of input parameters at the structural level

The effect of individual input parameters on resulting temperature field is explored in a closer detail. For this purpose, a half of bridge cross-section in Fig. 21 was taken, capturing different thermal evolution in a massive beam and a slender slab. Each of 84 quadrilateral finite elements with linear interpolation corresponds to 84 independent CEMHYD3D material models. Since no great accuracy is expected, only $25 \times 25 \times 25$ μm microstructures were used. The macroscopic model has 109 DoF.

The starting "normal" concrete composition is made from 300 kg of CEM I 42.5 R according to Tab. 2 with the activation energy $E_a = 38.3$ kJ/mol and $w/c = 0.5$. Besides, the variation of other parameters covered

- 400 and 200 kg of cement CEM I 42.5 R,
- increased Blaine fineness from 306 to 500 m^2/kg,

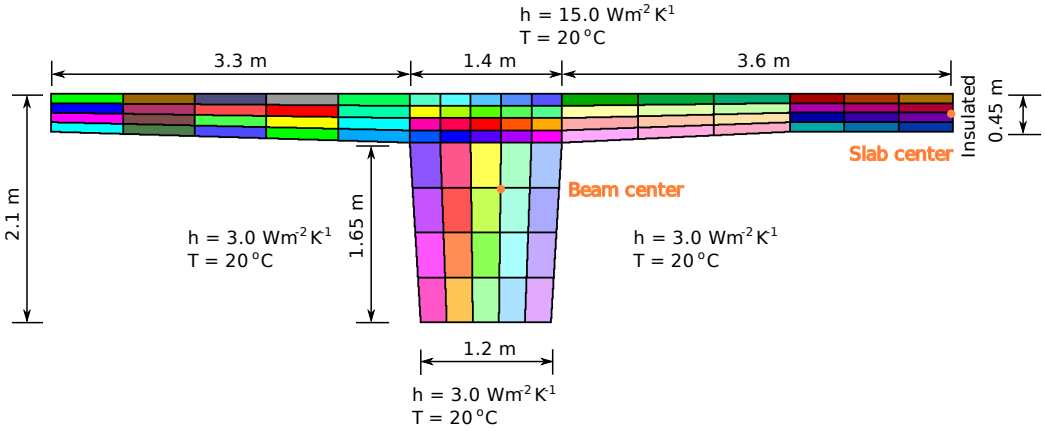

Figure 21: Topology of bridge cross-section with the mesh, boundary conditions and important node positions

- C_3S increased from original 68.30 % C_3S to 73 % by mass without gypsum, preserving the ratio of other clinker minerals and maintaining 5 % of gypsum addition by volume,
- w/c decreased from 0.5 to 0.3,
- initial mix temperature in the range from 0 to 30 °C surrounded by 20 °C ambient air temperature.

Fig. 22 indicates maximum temperatures in the beam and slab with corresponding elapsed time when $\beta = 7.8 \cdot 10^{-4}$ h and $t_0 = 0.0$ h. As expected, massive beam with the dimensions 1.2×2.1 m is close to adiabatic curing conditions while the slab is progressively cooled down by ambient air. Cement in the amount of 200 kg/m^3 may represent not only pure Portland cement but a hydrating part of blended cements. Hydration at $w/c = 0.3$ is slowed down in later stages due to water demand, resulting in decreased reaction kinetics. Low initial mix temperature is very beneficial in preventing excessive overheating and, in fact, represents a common mean found in various guidelines. A similar effect is expected from surrounding ambient air temperature which would reflect casting in different seasons.

The maximum temperature in the beam is achieved between 40 – 100 hours of hydration and demonstrates high influence of mix and curing conditions. Temperature in the slab 0.45 m thick is reached sooner for a given setup, approximately in the half time of the beam, i.e. in the interval 20 – 47 hours. It should be noted that cycle-time mapping parameter β could be lower which would cause time shortening of maximum temperature.

The computation took 46 minutes on 3.2 GHz PC and occupied 43 MB of RAM including all code, data and shared libraries. The simulation covered

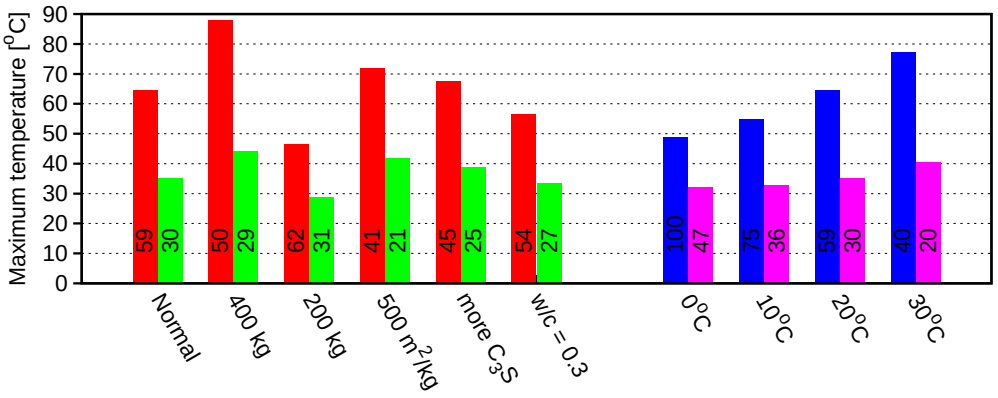

Figure 22: Maximum temperatures in the beam (left columns) and slab (right columns). Number in the bar represents time in hours when maximum temperature was reached

the period up to 5 days using 10 minute constant integration step.

7 Conclusion

This paper has presented a multiscale model with following conclusions

1. CEMHYD3D model was introduced with the description of the reconstruction of initial cement paste microstructure,
2. microstructure size of 50 × 50 × 50 μm is representative enough for heat analysis at the level of cement paste,
3. hydration model has to be calibrated by two parameters t_0 and β, reflecting additional effects such as alkalies or admixtures,
4. thermal conductivity and heat capacity of ordinary concrete does not vary significantly during hydration and the properties may be regarded constant,
5. validation shows perfect agreement in isothermal calorimetry,
6. validations on casted cube and bridge parts show reasonable temperature agreement and allow accessing the local quantities,
7. a typical bridge cross section is analyzed for maximum temperatures to shed a light on the effect of concrete and cement input parameters. Lower initial concrete temperature, lower w/c and lower cement amount act beneficially for maximum temperature depression,
8. proposed tool is generally applicable and extensible for a broad variety of conditions. It is well suited for engineering purposes and for optimization of a casting process in terms of temperature.

Acknowledgement

We gratefully acknowledge financial support from the grant MSM 6840770003. Bentz and Garboczi are acknowledged for CEMHYD3D hydration model.

References

[Barbarulo et al., 2005] Barbarulo, R., Peycelon, H., Prené, S., and Marchand, J. (2005). Delayed ettringite formation symptoms on mortars induced by high temperature due to cement heat of hydration or late thermal cycle. *Cem. Concr. Res.*, 35(1):125–131.

[Bentur and Mitchell, 2008] Bentur, A. and Mitchell, D. (2008). Material performance lessons. *Cem. Concr. Res.*, 38(2):259 – 272.

[Bentz, 1995] Bentz, D. (1995). A Three-Dimensional Cement Hydration and Microstructure Program. I. Hydration Rate, Heat of Hydration, and Chemical Shrinkage. Technical report, NIST Building and Fire Research Laboratory, Gaithersburg, Maryland.

[Bentz, 2000] Bentz, D. (2000). CEMHYD3D: A Three-Dimensional Cement Hydration and Microstructure Development Modeling Package. Version 2.0. Technical report, NIST Building and Fire Research Laboratory, Gaithersburg, Maryland.

[Bentz, 2008] Bentz, D. (2008). Transient Plane Source Measurements of the Thermal Properties of Hydrating Cement Pastes. *Materials and Structures*, submitted:to appear.

[Bentz, 2005] Bentz, D. P. (2005). CEMHYD3D: A Three-Dimensional Cement Hydration and Microstructure Development Modeling Package. Version 3.0. Technical report, NIST Building and Fire Research Laboratory, Gaithersburg, Maryland.

[Bentz et al., 1999] Bentz, D. P., Garboczi, E., Haecker, C., and Jensen, O. (1999). Effect of cement particle size distribution on performance properties of Portland cement-based materials. *Cem. Concr. Res.*, 29:1663–1671.

[Bentz et al., 1998] Bentz, D. P., Waller, V., and de Larrard, F. (1998). Prediction of Adiabatic Temperature Rise in Conventional and High-Performance Concretes Using a 3-D Microstructural Model. *Cem. Concr. Res.*, 28(2):285–297.

[Bernard et al., 2003] Bernard, O., Ulm, F.-J., and Lemarchand, E. (2003). A multiscale micromechanics-hydration model for the early-age elastic properties of cement-based materials. *Cem. Concr. Res.*, 33(9):1293–1309.

[Ch. Hellmich, 2001] Ch. Hellmich, H.A. Mang, F.-J. U. (2001). Hybrid method for quantification of stress states in shotcrete tunnel shells: combination of 3D in situ displacement measurements and thermochemoplastic material law. *Computers and Structures*, 79:2103 – 2115.

[Estrada et al., 2006] Estrada, C. F., Godoy, L. A., and Prato, T. (2006). Thermo-mechanical behavior of a thin concrete shell during its early age. *Thin-Walled Structures*, 44(5):483–495.

[Gawin et al., 2006a] Gawin, D., Pesavento, F., and Schrefler, B. (2006a). Hygro-thermo-chemo-mechanical modelling of concrete at early ages and beyond. Part I: Hydration and hygro-thermal phenomena. *International Journal for Numerical Methods in Engineering*, 67(3):299–331.

[Gawin et al., 2006b] Gawin, D., Pesavento, F., and Schrefler, B. (2006b). Hygro-thermo-chemo-mechanical modelling of concrete at early ages and beyond. Part II: shrinkage and creep of concrete. *International Journal for Numerical Methods in Engineering*, 67(3):332–363.

[Hughes, 2000] Hughes, T. (2000). *The Finite Element Method–Linear Static and Dynamic Finite Element Analysis*. Dover Publishers, New York.

[Kada-Benameur et al., 2000] Kada-Benameur, H., Wirquin, E., and Duthoit, B. (2000). Determination of apparent activation energy of concrete by isothermal calorimetry. *Cem. Concr. Res.*, 30(2):301–305.

[Kanit et al., 2003] Kanit, T., Forest, S., Galliet, I., Mounoury, V., and Jeulin, D. (2003). Determination of the size of the representative volume element for random composites: Statistical and numerical approach. *International Journal of Solids and Structures*, 40:3647–3679.

[Lienhard and Lienhard, 2008] Lienhard, J. and Lienhard, J. (2008). *A heat transfer textbook*. Phlogiston Press, Cambridge.

[Lothenbach et al., 2008] Lothenbach, B., Matschei, T., Möschner, G., and Glasser, F. (2008). Thermodynamic modelling of the effect of temperature on the hydration and porosity of Portland cement. *Cem. Concr. Res.*, 38(1):1–18.

[Maekawa et al., 1999] Maekawa, K., Chaube, R. P., and Kishi, T. (1999). *Modeling of Concrete Performance*. E & FN SPON (London), first edition.

[Neville, 1997] Neville, A. M. (1997). *Properties of Concrete*. John Wiley & Sons, Inc.

[Nilsson, 2000] Nilsson, M. (2000). *Thermal Cracking of Young Concrete. Partial Coefficients, Restraint Effects and Influence of Casting Joints*. Licentiate thesis, Luleå Univeristy of Technology.

[NRMCA, 2007] NRMCA (1978–2007). Concrete in practics. Technical report, National Ready Mixed Concrete Association.

[Pane and Hansen, 2005] Pane, I. and Hansen, W. (2005). Investigation of blended cement hydration by isothermal calorimetry and thermal analysis. *Cem. Concr. Res.*, 35(6):1155–1164.

[Papadakis, 1999] Papadakis, V. (1999). Effect of fly ash on Portland cement systems: Part I. Low-calcium fly ash. *Cem. Concr. Res.*, 29(11):1727–1736.

[Park et al., 2008] Park, K.-B., Jee, N.-Y., Yoon, I.-S., and Lee, H.-S. (2008). Prediction of Temperature Distribution in High-Strength Concrete Using Hydration Model. *ACI Materials Journal*, 105(2):180–186.

[Robeyst et al., 2007] Robeyst, N., Gruyaert, E., and Belie, N. D. (2007). *Advances in Construction Materials 2007: Ultrasonic and calorimetric measurements on fresh concrete with blast-furnace slag*, chapter VI, pages 497–504. Springer Berlin Heidelberg.

[Schrage and Summer, 1994] Schrage, I. and Summer, T. (1994). Factors influencing early cracking of high strength concrete. In Springenschmidt, R., editor, *Proceedings of International RILEM Symposium. Thermal Cracking in Concrete at Early Ages*, page 237–244, Munich, Germany.

[Snelson et al., 2008] Snelson, D. G., Wild, S., and O'Farrell, M. (2008). Heat of hydration of Portland Cement-Metakaolin-Fly ash (PC-MK-PFA) blends. *Cem. Concr. Res.*, 38(6):832–840.

[Ulm and Coussy, 1998] Ulm, F.-J. and Coussy, O. (1998). Couplings in early-age concrete: From material modeling to structural design. *International Journal of Solids and Structures*, 35(31–32):4295–4311.

[Šmilauer and Bittnar, 2006] Šmilauer, V. and Bittnar, Z. (2006). Microstructure-based micromechanical prediction of elastic properties in hydrating cement paste. *Cem. Concr. Res.*, 36(9):1708–1718.

[Wang and Mai, 2005] Wang, B.-L. and Mai, Y.-W. (2005). Transient one-dimensional heat conduction problems solved by finite element. *International Journal of Mechanical Sciences*, 47(2):303–317.

[Wang and Dilger, 1994] Wang, C. and Dilger, D. (1994). Prediction of temperature distribution in hardening concrete. In Springenschmidt, R., editor, *Proceedings of International RILEM Symposium. Thermal Cracking in Concrete at Early Ages*, pages 21–28, Munich, Germany.